

A 3D stochastic cloud model for investigating the radiative properties of inhomogeneous cirrus clouds

By ROBIN J. HOGAN* and SARAH F. KEW

Department of Meteorology, The University of Reading, UK

(Received 29 September 2004; revised 22 April 2005)

SUMMARY

The three-dimensional structure of clouds is known to be important for determining their radiative effects, but it is difficult to obtain this structure directly from observations. In this paper a stochastic model is described that is capable of simulating the structural properties unique to cirrus: fallstreak geometry and shear-induced mixing. We first present an analysis of time–height cloud radar sections from southern England to extract the cirrus parameters of interest. It is found that horizontal power spectra of the logarithm of ice-water content (estimated from radar reflectivity factor and temperature) typically exhibit a spectral slope of around $-5/3$ near cloud top that decreases with depth into the cloud, to values as low as -3.5 in some cases. This decrease can be explained by wind shear coupled with a spread of particle fall speeds leading to a homogenization that acts preferentially at smaller scales. The power spectra exhibit a distinct scale break, becoming flat at scales larger than around 50 km (the ‘outer scale’). The orientation of the fallstreaks may be predicted from the profile of mean wind and mean ice fall speed. We then describe the stochastic model, which takes as input profiles of the mean and fractional standard deviation of ice-water content, spectral slope, outer scale and wind speed. It first generates an isotropic 3-D fractal field by performing an inverse 3-D Fourier transform on a matrix of simulated Fourier coefficients with amplitudes consistent with the observed 1-D spectra. Random phases for the coefficients allow multiple realizations of a cloud with the same statistical properties to be generated. Then horizontal slices from the domain are manipulated in turn to simulate horizontal displacement and changes to the spectra with height. Finally the field is scaled to produce the observed mean and fractional standard deviation of ice-water content. Vertical 2-D slices extracted from the domain are very similar in appearance to cloud radar observations. Radiative-transfer calculations using the independent column approximation are used to show that the different fallstreak orientation resulting from different wind shears can change mean top-of-atmosphere radiative fluxes by in excess of 45 W m^{-2} in the short-wave and 15 W m^{-2} in the long-wave. The effect of wind shear to induce horizontal mixing causes an additional but smaller radiative effect. We also investigate the biases that would be expected from the assumptions made in the radiation schemes of general-circulation models (GCMs). It is found that there is some compensation between the errors arising from the assumptions of horizontal homogeneity and maximum-random overlap; if a GCM were to improve the overlap assumption but still assume clouds to be horizontally homogeneous then the total error in cloud radiative effect would be likely to increase.

KEYWORDS: Cirrus uncinus Cloud heterogeneity Cloud overlap Fractal

1. INTRODUCTION

The importance of ice clouds on the earth’s radiation budget is well recognized (e.g. Liou 1986), and studies have shown that ice-cloud inhomogeneity can have a strong effect on mean fluxes in both the long-wave (Pomroy and Illingworth 2000; Fu *et al.* 2000) and short-wave (Carlin *et al.* 2002; Buschmann *et al.* 2002). Observations that

* Corresponding author: Department of Meteorology, The University of Reading, Earley Gate, PO Box 243, Reading RG6 6BB, UK. e-mail: r.j.hogan@reading.ac.uk

have quantified ice-cloud inhomogeneity have tended to be essentially either one- or two-dimensional, such as from satellite (Kuo *et al.* 1988), aircraft (Smith and DelGenio 2001) and cloud radar (Hogan and Illingworth 2003), but the three-dimensional structure is required for comprehensive radiative-transfer calculations. Cloud-resolving model simulations have yet to demonstrate the ability to simulate realistic cirrus fallstreak structures, and are also very expensive to run in large 3-D domains.

Stochastic models capable of simulating realistic 3-D cloud structures are very useful for quantifying cloud radiative effects, and several such models exist for boundary-layer clouds, such as that of DiGiuseppe and Tompkins (2003) for stratocumulus, and Evans and Wiscombe (2004) for cumulus (numerous other 2-D models exist). In this paper we present the first stochastic model capable of representing the important structural properties unique to cirrus: fallstreak geometry and shear-induced mixing. The model essentially takes the characteristic slope and scale break from 1-D power spectra of ice-water content obtained from cloud radar, and performs a 3-D inverse Fourier transform on a matrix of simulated Fourier amplitudes with random phases to obtain an isotropic 3-D fractal field with the same spectral properties as the original data. Each vertical layer of the field is then manipulated in various ways to generate a realistic cirrus cloud. A simpler approach in two dimensions was taken by Hogan and Illingworth (1999) to estimate the error to be expected for two active cloud remote sensors (e.g. radar and lidar) on different satellite platforms, due to mismatched sample volumes.

In section 2 we analyse cloud radar data to extract the parameters describing the 3-D structure of cirrus, and in section 3 the formulation of the model is described. In section 4, three cirrus cases are used to demonstrate the performance of the model, and in section 5, radiation calculations are performed to investigate the effect of cloud structure on mean fluxes and heating rates.

2. ANALYSIS OF CLOUD RADAR DATA

We use data recorded by the vertically pointing 94 GHz Galileo radar located at Chilbolton in southern England to extract the parameters required by the stochastic model. The radar was calibrated to an accuracy of around 1.5 dB by comparison with the weather radar at Chilbolton, as described by Hogan *et al.* (2003). An additional 2 dB was added to the reflectivity field to account approximately for the attenuation by atmospheric gases to cirrus altitudes. The radar has a vertical resolution of 60 m and the data were averaged to 30 s in time. We initially study a cirrus cloud observed on 27 December 1999. Other cases are considered in section 4.

(a) Probability density function

The reflectivity field Z (dBZ) is converted to ice-water content IWC (g m^{-3}), using the formula appropriate for estimating the ‘unbiased variance and probability density function’ given by Hogan *et al.* (2005):

$$\log_{10} \text{IWC} = 0.085Z - 0.0189T - 1.19, \quad (1)$$

where T is temperature ($^{\circ}\text{C}$). Figure 1 shows a time–height cross-section of derived IWC for the cloud on 27 December 1999. From the same case Hogan and Illingworth (2003) found that the probability density function (PDF) of IWC could usually be well represented by a log-normal distribution. They characterized the horizontal variability

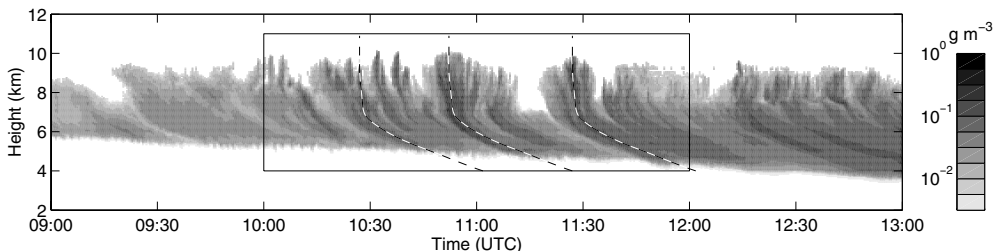


Figure 1. Ice-water content derived from the 94 GHz radar at Chilbolton on 27 December 1999. The box between 10 and 12 UTC indicates the period analysed to extract parameters from which the stochastic cloud model could be run. The black-and-white dashed lines indicate the trajectories of fallstreaks predicted from the radiosonde wind profile assuming a generating level of 9.1 km and a constant fall speed of 0.8 m s^{-1} (see section 3(b)).

in terms of the fractional variance of IWC, which may be regarded as the variance of $\ln \text{IWC}$. We therefore constrain the stochastic model to produce at each height log-normal IWC distributions with mean and fractional standard deviation ($\overline{\ln \text{IWC}}$ and $\sigma_{\ln \text{IWC}}$) derived from the radar data. Where there are gaps in the radar data due to reflectivities below the instrument sensitivity threshold (or indeed due to cloud-free air), the data are analysed in such a way as to obtain the parameters of an ‘underlying’ log-normal distribution which best fits the observed PDF in the upper part of its range. This procedure is described in appendix A.

The stochastic model generates clouds that are periodic in both the x and y directions, so is unable to represent systematic changes in cloud depth from one side of the domain to the other. It is therefore best to restrict analysis of radar data to periods over which cloud evolution is weak. Due to the descent of cloud base over the four hours shown in Fig. 1, we restrict our analysis to the period 10–12 UTC, indicated by the box. Figure 2(a) shows cloud fraction (denoted f in appendix A) versus height from this box, at the radar vertical resolution of 60 m. Figures 2(c) and (d) depict the parameters describing the PDF, with the solid lines showing $\overline{\ln \text{IWC}}$ and $\sigma_{\ln \text{IWC}}$ for the cloudy pixels, and the dashed lines the same but for the underlying distribution after applying vertical smoothing to reduce sampling noise. As cloud fraction decreases, $\overline{\ln \text{IWC}}$ of the underlying distribution must decrease and the corresponding $\sigma_{\ln \text{IWC}}$ increase relative to the in-cloud values in order that the measured distribution is reproduced. Care needs to be taken near cloud top and base because the method for deriving the parameters of the underlying distribution can produce rather noisy results when cloud fraction is small. In this case we choose to restrict the simulation only to the height range for which $f > 0.2$. Additionally, the horizontal PDF can deviate from log-normal close to cloud base due to a combination of descending cloud-base height with time and small-scale convective overturning (Hogan and Illingworth 2003). As the model is currently not formulated to represent PDFs other than log-normal, we impose the additional constraint that $\sigma_{\ln \text{IWC}}$ should not exceed 1.5 within 1 km of cloud base. As will be seen in section 4, this prevents some of the detailed features of cloud base from being simulated, but they are not believed to be radiatively significant so this is not a serious shortcoming.

(b) Vertical structure

A striking feature of radar images of ice clouds, not least Fig. 1, is the fallstreak structure, whereby horizontal inhomogeneities caused by convective overturning at cloud top (the ‘generating level’) are carried down with the falling ice, but displaced horizontally with respect to cloud top due to the presence of vertical wind shear.

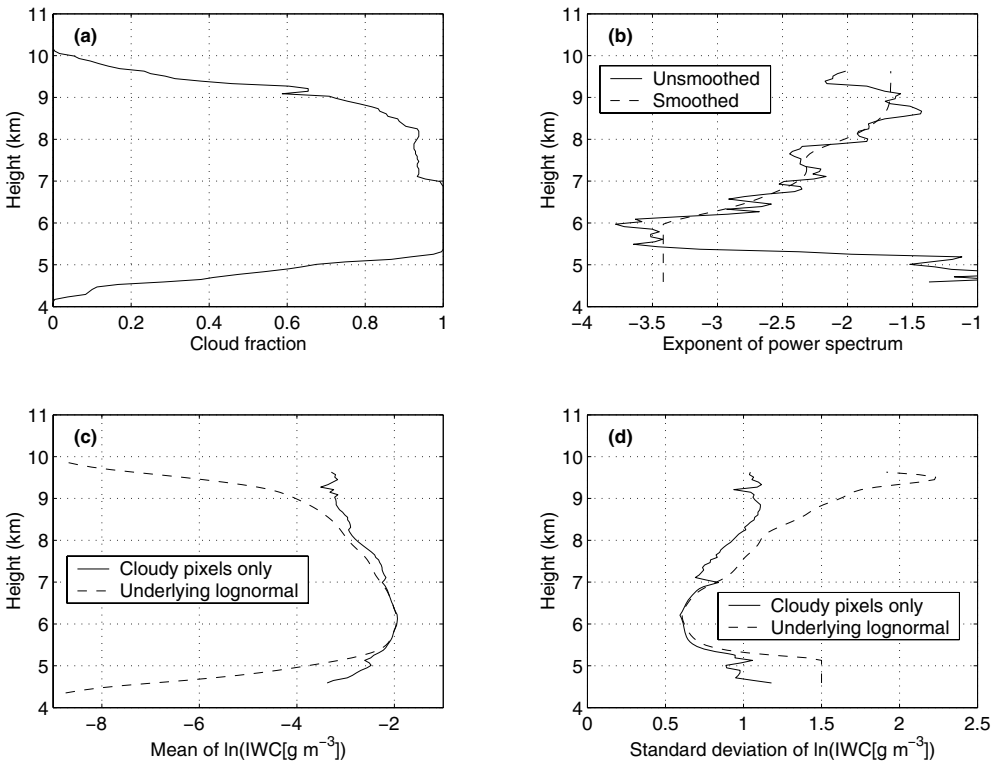


Figure 2. Parameters, derived from the 27 December 1999 radar data between 10 and 12 UTC, as a function of height: (a) cloud fraction, (b) power spectral slope for scales smaller than 50 km, where the solid line indicates the values calculated from the spectra at each height and the dashed line indicates the smoothed values used by the stochastic model, (c) mean of \ln IWC for the cloudy pixels (solid line) and the inferred (and smoothed) mean of the ‘underlying’ log-normal distribution, and (d) standard deviation of \ln IWC for both the cloudy pixels and the underlying distribution.

We may predict the 3-D trajectories of fallstreaks by consideration of the horizontal wind profile (u , v), the profile of mean ice fall speed w and the height of the generating level z_{gen} following Marshall (1953). In time dt an ice particle at height z is advected in the x direction a distance $u(z) dt$, while the generating cell above it (from which particles are still falling) moves a distance $u(z_{\text{gen}}) dt$. Thus the change in distance from the generating level is $dx = (u(z) - u(z_{\text{gen}})) dt$. Noting that the ice fall speed is given by $w = dz/dt$, the orientation of the fallstreak in the x direction is therefore given by

$$dx/dz = (u(z) - u(z_{\text{gen}}))/w(z). \quad (2)$$

The equation for dy/dz follows in the same way. Marshall (1953) then showed that the assumption of constant vertical wind shear and constant particle fall speed led to parabolic fallstreaks, i.e. the horizontal distance from the generating cell being proportional to the square of the distance fallen. Recently, Mittermaier *et al.* (2004) used this approach to predict the horizontal distribution of surface rainfall given a horizontal weather radar scan at the height of the ice fallstreaks.

In this paper a more realistic horizontal displacement profile (x , y) is calculated using the finite difference equivalent of (2), starting at the generating level and working downwards. Thus the x displacement at level i is given as a function of the displacement

at the level above $i + 1$, by

$$x_i = x_{i+1} + (u_i + u_{i+1} - 2u(z_{\text{gen}}))(z_i - z_{i+1})/(w_i + w_{i+1}), \quad (3)$$

and similarly for y_i . Note that u and w have been represented as the average of the values at levels i and $i + 1$. This model may be tested on the case from 27 December 1999, for which the wind shear vector was almost parallel to the wind vector at the height of the generating level resulting in entire fallstreaks being within the plane of the time–height sections from a single location. The dashed lines in Fig. 1 show the predicted fallstreak trajectories from the wind profile measured by radiosonde launched at 11 UTC from Herstmonceux, 125 km from Chilbolton, and assuming a generating level of $z_{\text{gen}} = 9.1$ km (with zero horizontal displacement above) and a constant fall speed of 0.8 m s^{-1} . The predicted horizontal displacement has been converted to an equivalent time using the wind velocity at z_{gen} of 56 m s^{-1} . These subjectively chosen values of z_{gen} and w result in the trajectories of the observed fallstreaks in the IWC field being predicted very well. In principle the velocity measured by a Doppler radar could be used for w , but the success of a constant value suggests that it would not be a significant advantage.

(c) *Horizontal structure*

The horizontal structure is characterized by taking power spectra of \ln IWC at each height. The radar data are first transformed from time to horizontal distance using the wind at the height of the generating level. Gaps in the data are replaced by a constant value below the radar sensitivity threshold.

The results for the cloud in Fig. 1 are shown in Fig. 3, calculated using the full four hours of data. It can be seen that near cloud top a spectral slope of $-5/3$ is evident. This indicates that here IWC is acting as a tracer of a turbulent field, presumably originating from convective overturning in the generating region. The fact that this behaviour is seen up to scales of 50–100 km indicates a 2-D upscale cascade of energy (e.g. Lilly 1983) rather than 3-D turbulence in the inertial subrange, although interaction with gravity waves could play a part. The reason for a scale break at 50–100 km is not certain, although it was clearly also evident in the fractional variance results of Hogan and Illingworth (2003), obtained from 18 months of data. For this to occur there has to be a process acting to prevent very high IWC values. A possible mechanism is simply that high IWC will correspond to faster falling particles, resulting in more rapid loss of ice by sedimentation.

Below cloud top there is a distinct steepening of the power spectra, indicating the suppression of structure preferentially at small scales. An explanation for this is variable particle fall speeds in the presence of vertical wind shear leading to different horizontal displacements (as predicted by (3)) and hence a horizontal homogenization. This also has the effect of reducing the fractional variance towards the interior of the cloud, as seen in Fig. 2(d) and reported by Hogan and Illingworth (2003).

The parameters of the spectrum provided to the stochastic model are simply the slope of the power spectrum at each height and the position of the scale break, which is assumed constant with height. It will be seen in the next section that it is easy to simulate the smooth roll-off towards a flat spectrum at scales larger than the scale break. It should be noted that the absolute value of spectral energy does not need to be recorded, as this is implicitly provided by the fractional variance $\sigma_{\ln \text{IWC}}^2$ which, by Parseval's Theorem, is simply the area under the power spectrum. The slope of the power spectrum is shown in Fig. 2(b), this time calculated for the same 10–12 UTC period as used for the other

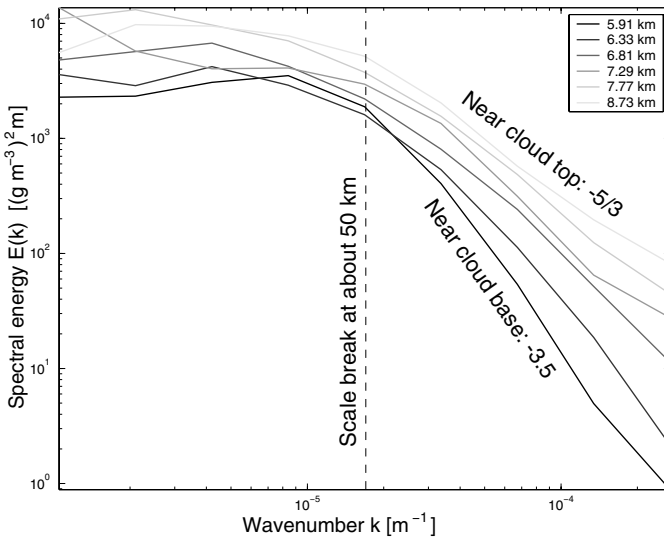


Figure 3. Power spectra of \ln IWC as a function of height for the data shown in Fig. 1. The raw spectra have been averaged such that there are around four points per decade of wave number. Note that wave number is defined here as the reciprocal of wavelength.

parameters, resulting in a somewhat noisier profile. The dashed line shows the smoothed profile provided to the stochastic model. At cloud top the spectra are unreliable due to the low cloud fraction, so here the slope is relaxed to a value of $-5/3$. At cloud base, where the PDF can deviate from log-normal, the spectrum is also unreliable, so here slope is forced to a constant value corresponding to the value at 6 km.

3. FORMULATION OF THE STOCHASTIC CLOUD MODEL

The stochastic model takes as input profiles of the following parameters derived from radar observations: the mean and standard deviation of the underlying \ln IWC distribution, the horizontal wind components, the ice fall speed and the slope of the \ln IWC power spectrum. In addition, the scalar parameters it requires are the outer scale, the generating-level height (chosen subjectively) and the threshold IWC for defining cloud boundaries.

(a) Generation of an isotropic fractal field

The first step is to generate a 3-D isotropic field $g(x, y, z)$ with a Gaussian PDF and a spectral slope to reflect the observations at a particular height. Suppose that we wish the 1-D power spectrum $E_1(k)$ through this field to have a single slope $-\mu$ at all scales:

$$E_1(k) = \widehat{E}_1 k^{-\mu}, \quad (4)$$

where k is wave number in any direction and \widehat{E}_1 is the spectral energy density at $k = 1 \text{ m}^{-1}$. Note that throughout this paper we adopt the convention that $k = 1/\lambda$ (where λ is wavelength) rather than $k = 2\pi/\lambda$. Now, for the 3-D field we are to generate, there exists a 3-D spectral energy density matrix $E_3(k_x, k_y, k_z)$, which is found by taking the 3-D discrete Fourier transform of g and multiplying each resulting Fourier amplitude by its complex conjugate (i.e. taking the square of the amplitude and discarding the phase information). Our approach is to reverse this process: if we can somehow generate E_3

then, by assuming random phases for each of the Fourier amplitudes, a 3-D inverse Fourier transform will yield the required fractal field. The Fourier amplitudes are generated by multiplying the square root of each element of E_3 by a complex number with random real and imaginary parts drawn from a Gaussian distribution with a mean of zero and a standard deviation of unity. A different set of random numbers will produce a different realization of the cloud field, but with the same statistical properties.

So how can E_3 be derived from E_1 ? Physically, $E_3(k_x, k_y, k_z) dk_x dk_y dk_z$ is the spectral energy of a wave directed in a particular direction in 3-D space. If a one-dimensional sample were taken through this single wave in, say, the x direction, then a spectral energy E_1 would be measured at wave number k_x such that $E_1(k_x) dk_x = E_3(k_x, k_y, k_z) dk_x dk_y dk_z$. Since all 3-D wave components with an x -wave number of k_x will contribute to $E_1(k_x)$, and the energies (or equivalently the variances) of waves with uncorrelated phases should sum linearly, we obtain a general expression for a 1-D power spectrum through g in the x direction:

$$E_1(k_x) = \int_{-\infty}^{\infty} \int_{-\infty}^{\infty} E_3(k_x, k_y, k_z) dk_y dk_z, \quad (5)$$

and similarly in the y and z directions. For g to be isotropic, E_3 must be a function of absolute wave number $k = (k_x^2 + k_y^2 + k_z^2)^{1/2}$ only. In the idealized case that g is continuous at small scales and infinite in extent, (4) and (5) have the solution

$$E_3(k) = \frac{\widehat{E}_1 \mu}{2\pi} k^{-\mu-2}, \quad (6)$$

i.e. the 3-D power spectrum is a simple power law and is steeper than E_1 by two powers of k . Equation (6) may be applied satisfactorily to discrete fields of finite horizontal extent, provided that both the domain size and grid spacing are the same in each direction. However, in simulations of cirrus we require a much larger domain in the horizontal than the vertical (at least as large as the outer scale) and a high resolution in the vertical to resolve the fallstreaks. In this case, when (5) is reduced to a discrete summation, there is no longer a simple analytical solution for E_3 . Instead we find an approximate solution by dividing absolute wave-number space into a number of separate regions each with a separate power law. This also allows the scale break found in the observations to be incorporated into the solution.

The domain of the cloud field is defined to measure L_x , L_y and L_z and have resolutions of Δx , Δy and Δz in the x , y and z directions respectively. Typically the values of these parameters would be chosen to ensure that the number of grid points in each direction is an integer power of two, to maximize the efficiency of the fast Fourier transform. The resulting wave-number domain for E_3 ranges from $-K_x$ to $+K_x$ with a resolution of Δk_x in the k_x direction, where $K_x = (2\Delta x)^{-1}$ and $\Delta k_x = L_x^{-1}$, and similarly for the k_y and k_z directions. From here on we use the same resolution and domain size in the x and y directions, i.e. $L_x = L_y$, $K_x = K_y$, etc. The outer scale observed in the radar power spectra is characterized by its wave number k_{outer} . The result is that E_3 may be well represented by four regions of k space as follows:

$$E_3 = \frac{\widehat{E}_1}{\Delta k_z \sqrt{\pi}} \frac{\Gamma\{(\mu+1)/2\}}{\Gamma(\mu/2)} k_{\text{outer}}^{-\mu-1}, \quad k \leq k_{\text{I}} \text{ (Region I)}, \quad (7)$$

$$E_3 = \frac{\widehat{E}_1}{\Delta k_z \sqrt{\pi}} \frac{\Gamma\{(\mu+1)/2\}}{\Gamma(\mu/2)} k^{-\mu-1}, \quad k_{\text{I}} < k \leq k_{\text{II}} \text{ (Region II)}, \quad (8)$$

$$E_3 = \frac{\widehat{E}_1 \mu}{2\pi} k^{-\mu-2}, \quad k_{\text{II}} < k \leq k_{\text{III}} \text{ (Region III)}, \quad (9)$$

$$E_3 = \frac{\widehat{E}_1}{4K_x K_y} k^{-\mu}, \quad k_{\text{III}} < k \text{ (Region IV)}, \quad (10)$$

where the boundaries between the regions are defined as

$$k_{\text{I}} = k_{\text{outer}}, \quad (11)$$

$$k_{\text{II}} = \frac{\mu}{2\sqrt{\pi}} \frac{\Gamma(\mu/2)}{\Gamma\{(\mu+1)/2\}} \Delta k_z, \quad (12)$$

$$k_{\text{III}} = \sqrt{2\mu/\pi} K_x, \quad (13)$$

and Γ denotes the gamma function. These expressions are derived in appendix B. We set $E_3 = 0$ for $k = 0$ in order that the resulting field has a mean of zero.

Figure 4 illustrates the generation of a 3-D fractal field in ‘quasi-schematic’ form, i.e. the full method has been used to generate these plots, but the parameters such as resolution and domain size have been chosen to best illustrate the procedure and are not relevant to the discussion. The locations of the four regions in wave-number space are shown in Fig. 4(a), where the dots represent individual points on the discrete wave-number grid and are a distance $\Delta k_x = \Delta k_y$ apart in the x and y directions and Δk_z apart in the z direction. Figure 4(b) depicts E_3 versus absolute wave number k in log-log space, as defined in (7)–(13). The corresponding E_1 spectrum is shown in Fig. 4(c), with the grey line representing the ‘requested’ 1-D spectrum while the black lines show the 1-D spectra of the simulation in the x and z directions as calculated by simple integration using (5). Note that the latter should be regarded as long-term averaged power spectra from many realizations of the field; individual power spectra from particular realizations exhibit significant point-to-point variability. It can be seen that the agreement is good, validating the approximation of dividing E_3 into four regions with constant slopes. The use of a constant value for E_3 in Region I results in a smooth roll-off of the slope when the outer scale is reached, very similar to the observed power spectra in Fig. 3. A realization of the fractal field is shown in Fig. 4(d). It should be noted that Fig. 4 was calculated for $\mu = 2$, and the agreement evident in Fig. 4(c) is better for larger values of μ but poorer for lower values.

(b) Conversion to a realistic cloud field

The 3-D fractal field is manipulated in various ways to simulate a realistic cirrus cloud. The first two steps, horizontal displacement (to simulate fallstreaks) and adjustment of the slope of the power spectrum (to simulate shear-induced mixing) are performed in the wave-number domain. Layers are analysed in turn, with a 2-D Fourier transform performed at each height resulting in a 2-D plane of Fourier amplitudes. In this context, absolute wave number is a function of the wave-number components in the x and y directions: $k = (k_x^2 + k_y^2)^{1/2}$.

Horizontal translation is straightforward to implement. If the fallstreak model of (3) predicts a horizontal translation of $(\delta x, \delta y)$ relative to the generating level, then we simply multiply each Fourier amplitude by $\exp(i\phi)$, where $\phi = 2\pi(k_x \delta x + k_y \delta y)$. No horizontal translation is performed above the generating layer. The model is therefore unable to represent the hook structure of cirrus generating cells as described by Heymsfield (1975).

In simulating mixing it is assumed that the 1-D power spectrum changes slope only at scales smaller than the outer scale, i.e. the power spectrum pivots from the point at

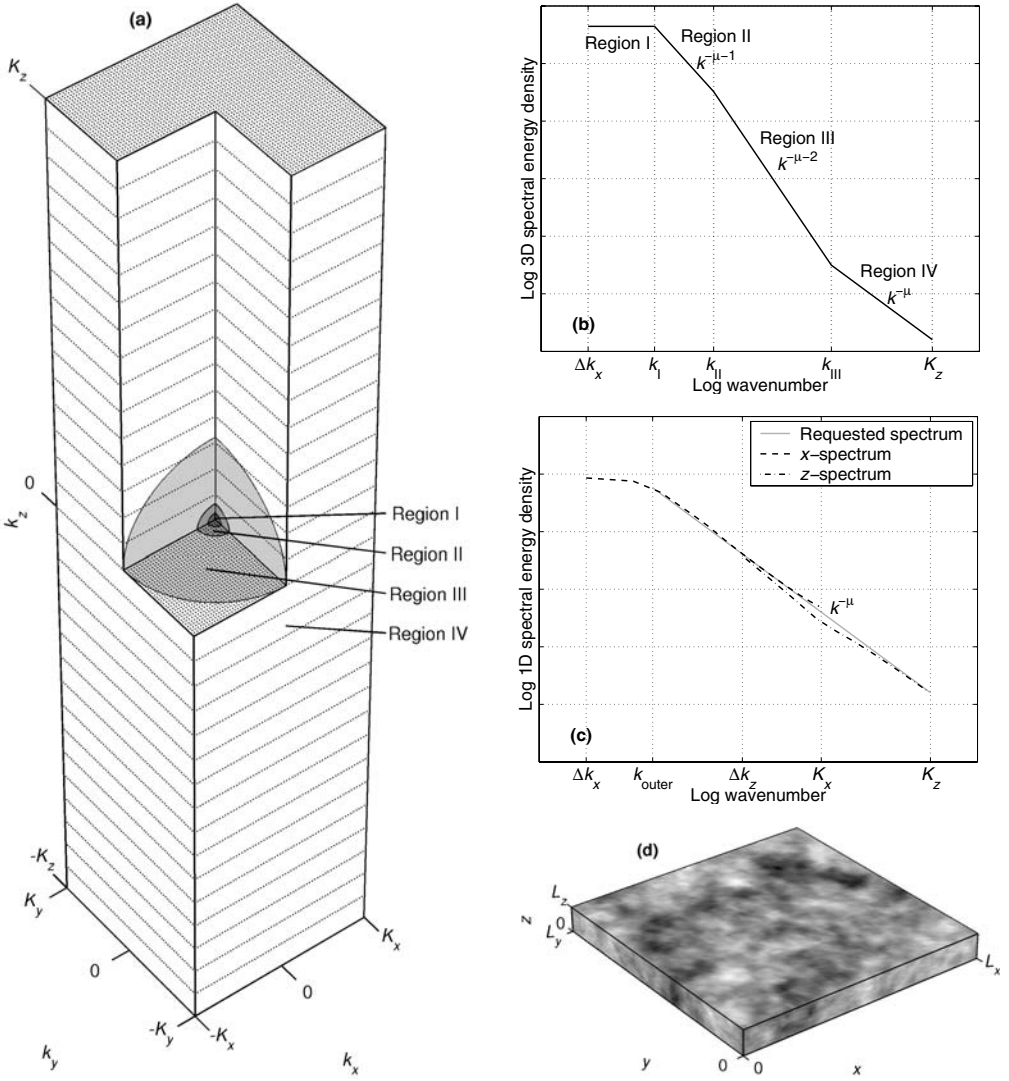


Figure 4. Schematic illustrating the generation of an isotropic fractal field on a non-uniform grid: (a) the discrete grid points in 3-D wave-number space, with the four spectral-slope regions I–IV indicated, (b) E_3 versus absolute wave number in each of the four regions, where $-\mu$ is the slope of the 1-D power spectrum, (c) average 1-D power spectra in the x and z directions over many realizations of the fractal field, together with the ‘requested’ 1-D spectrum E_1 , and (d) realization of an isotropic fractal field generated from E_3 . See text for explanation.

$k = k_{outer}$ in Fig. 4(c). To change the slope from $-\mu_1$ to $-\mu_2$, the Fourier amplitudes with $k > k_{outer}$ are multiplied by $(k/k_{outer})^{(\mu_1-\mu_2)/2}$, whilst those with $k \leq k_{outer}$ are left unchanged. Note that the power of one half is present because the operations are performed on the Fourier amplitudes, the square-roots of the power spectral densities. The mixing achieved by this operation is illustrated in Figs. 5(a) and 5(b).

It could be argued that this mixing model is not very realistic as it is isotropic, whereas in reality the homogenization might be expected to occur preferentially in the direction parallel to the wind shear vector. To simulate anisotropic mixing in the direction θ (measured anti-clockwise from the x axis), we define the wave number in

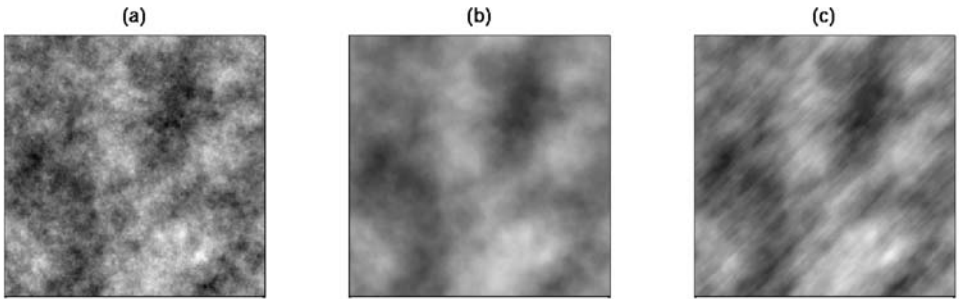


Figure 5. Illustration of the simulation of mixing by changing the spectral slope: (a) a 2-D field with a 1-D spectral slope of $-5/3$ and an outer scale equal to half the size of the domain, (b) the same field after reducing the Fourier amplitudes to obtain a spectral slope of -3 , and (c) simulation of anisotropic mixing by changing the spectral slope to -3 only in one direction.

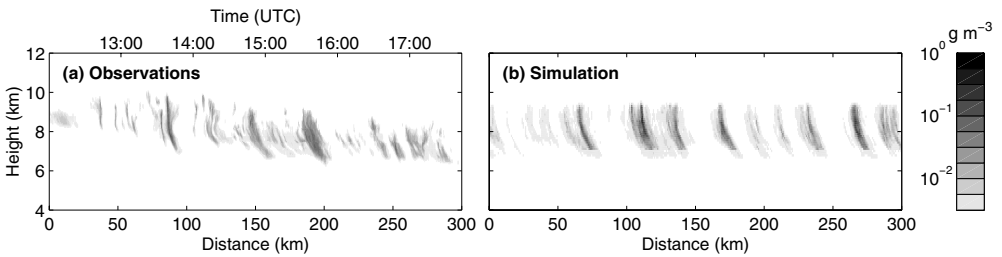


Figure 6. (a) Ice-water content derived from radar observations on 24 June 1999 versus both time and equivalent horizontal distance, and (b) a slice through a 3-D simulation of the same case at an angle parallel to the wind at the generating-level height.

this direction as $k_\theta = k_x \cos \theta + k_y \sin \theta$. The Fourier amplitudes with $k_\theta > k_{\text{outer}}$ are then multiplied by $(|k_\theta|/k_{\text{outer}})^{(\mu_1 - \mu_2)/2}$. The result is shown in Fig. 5(c) for $\theta = 45^\circ$. However, it has yet to be demonstrated from observations that cirrus fallstreaks act to mix anisotropically in this way, so isotropic mixing is used for the simulations in this paper.

After horizontal translation and mixing have been simulated in the wave-number domain, an inverse 2-D Fourier transform is performed to recover the modified field. At this stage the field has an approximately Gaussian distribution with a mean of zero and an arbitrary variance. The final step is to scale it and apply a threshold. We scale each 2-D slice of the field in order that it has the standard deviation $\sigma_{\ln \text{IWC}}$ obtained from observations. It should be noted that this scaling means that there is no need to ensure that the value of \widehat{E}_1 in (7)–(10) is correct. The resulting field is exponentiated to yield a log-normal distribution, and scaled again to obtain the required profile of $\ln \text{IWC}$ (or IWC) with height. Finally, values below a certain threshold may be set to zero to represent gaps in the cloud.

4. COMPARISON OF SIMULATIONS WITH ORIGINAL RADAR DATA

The model has been applied to three radar-observed cirrus clouds, including the 27 December 1999 case analysed previously. The radar-derived IWC fields are shown in Figs. 6(a), 7(a) and 8(a), with time converted to horizontal distance using the wind at the (subjectively determined) generating-level height. The clouds have progressively

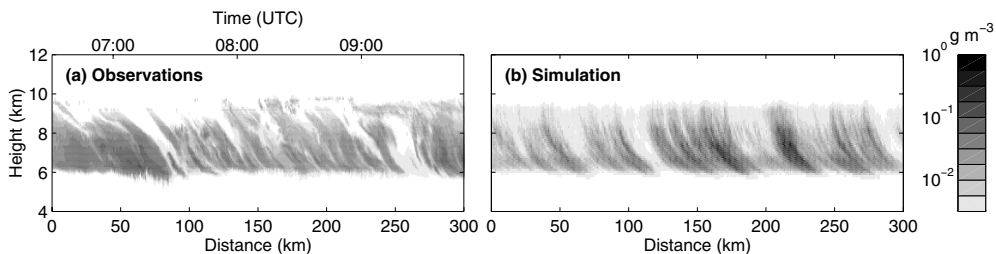


Figure 7. As Fig. 6 but for 27 August 1999.

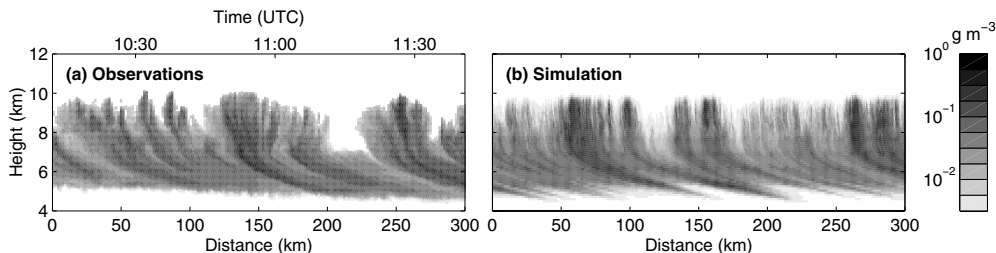


Figure 8. As Fig. 6 but for 27 December 1999.

TABLE 1. SUMMARY OF THE PROPERTIES OF THE CLOUDS SIMULATED IN SECTION 4 AND PLOTTED IN FIGS. 6–8. WIND SHEAR HAS BEEN CALCULATED OVER THE HEIGHT RANGE CORRESPONDING TO THE 25TH AND 75TH PERCENTILES OF HORIZONTAL-MEAN IWC. NOTE THAT μ WAS FOUND TO BE CLOSE TO $5/3$ AT CLOUD TOP IN ALL THREE CASES. DOMAIN-MEAN OPTICAL DEPTH (INCLUDING CLEAR-SKY REGIONS) WAS CALCULATED FROM $\delta = 3\text{IWP}/2\rho_i r_e$, WHERE ρ_i IS THE DENSITY OF SOLID ICE AND IWP IS ICE-WATER PATH, THE VERTICAL INTEGRAL OF IWC, AND r_e IS EFFECTIVE RADIUS.

Case	24 June 1999	27 Aug 1999	27 Dec 1999
Radars analysis period	12–18 UTC	06–11 UTC	10–12 UTC
Wind shear ($\text{m s}^{-1}\text{km}^{-1}$)	3.5	5.0	15.1
Generating-level height (km)	9.0	9.2	9.1
Generating-level wind (m s^{-1})	15	25	56
Outer scale (km)	30	50	50
Spectral slope coefficient (μ) at cloud base	2.4	2.8	3.4
Max. cloud fraction ($\text{IWC} > 10^{-3} \text{ g m}^{-3}$) at any height	0.51	1.00	1.00
Domain-mean visible optical depth for $r_e = 50 \mu\text{m}$	1.2	5.7	21.9

See text for further explanation.

increasing mean IWC, and are used in the next section to investigate the impact of cloud structure on radiative transfer over a range of conditions. The properties of the clouds were derived as described in section 2, and are summarized in Table 1. As was found with the 27 December 1999 case, the other two cases both exhibited a power spectral slope of close to $-5/3$ near cloud top that decreased further into the cloud. However, due to the reduced wind shear and hence reduced mixing, the slopes at cloud base were shallower, reaching -2.4 on 24 June 1999 and -2.8 on 27 August 1999.

Each simulation by the model was performed on a domain measuring $200 \text{ km} \times 200 \text{ km} \times 7 \text{ km}$, with a resolution of $256 \times 256 \times 64$ pixels. A constant fall speed of 0.8 m s^{-1} was assumed, with a threshold IWC of 10^{-3} g m^{-3} . Figures 6(b), 7(b) and 8(b) show slices through the 3-D simulations, extracted at an angle parallel to the

generating-level wind to represent what would be observed from a single point on the ground. The fact that slices were taken at an angle to the x - and y -axes means that they are non-repeating, even though the domain is periodic and they are longer than the 200 km domain size.

It can be seen that the dominant structures are captured well, in particular the orientation and typical spacing of fallstreaks. The first case from 24 June 2004 consisted of broken cirrus uncinus, and due to the low cloud fraction, parameters were derived from the observations for all layers with $f > 0.05$, rather than the 0.2 used for the other two cases (see section 2). The simulation is realistic despite the fact that the time series from which horizontal power spectra were derived consisted predominantly of constant ‘fill values’ below the radar sensitivity threshold. In the second case, from 27 August 1999, the cloud fraction appears to be greater in the simulation than in the observations. This is because the 10^{-3} g m^{-3} threshold is less than half the minimum detectable value by the radar at 10 km, so in fitting a log-normal distribution as described in appendix A, the simulation has essentially extrapolated the PDF to clouds that it assumes the radar is unable to detect. We find that this does not significantly affect the radiative-transfer calculations in the next section, as these low values are radiatively insignificant.

Power spectra through the simulated \ln IWC fields confirm that they are very similar to those through the original data, although this is hardly a surprise as it is one of the intrinsic properties of the model. However, there are differences in the morphology apparent to the eye but beyond those that can be revealed by power spectra. This includes systematic changes to particular cloud properties over the radar observation period, such as cloud-base height (Fig. 6(a)), fallstreak homogeneity (Fig. 7(a)) and fallstreak orientation (Fig. 8(a)). This non-stationary behaviour cannot be easily represented using a Fourier approach, which is intrinsically both periodic and statistically homogeneous in the horizontal plane. There is an additional difference in the ‘texture’ of the images, which can be attributed to the fact that rather different looking fields can yield the same power spectrum (Davis *et al.* 1996). The stochastic model of this paper has essentially produced a ‘monofractal’ realization of the observed cirrus cloud that lacks some of the ‘multifractal’ properties such as intermittency and non-stationarity. While parameters such as structure functions may be calculated from the observations to characterize aspects of multifractal behaviour (Marshak *et al.* 1997), we are left with the problem that rather different looking fields may also have the same multifractal properties. For example, the stochastic ‘bounded cascade’ model of Cahalan *et al.* (1994) can reproduce structure functions similar to those of geophysical fields, but the intermittency produced tends to be regularly spaced such that the discontinuities occur in the form of perfect squares, which is uncharacteristic of real clouds. A stochastic model has yet to be formulated that can pass the ‘Turing test’ of generating clouds that are indistinguishable from the real thing, but the important question is really whether such details have a significant effect on radiative properties. We contend that the larger-scale structures of cirrus, likely to dominate radiative transfer, are sufficiently well represented by a monofractal approach that a more complicated (and much less computationally efficient) multifractal model is not required.

Figure 9 shows a 3-D visualization of the simulation of the 27 December case, and the structure of individual fallstreaks is clearly evident. Near cloud top it can be seen that the field is horizontally isotropic, while in real cirrus gravity waves and shear can lead to roll-like structures in this region. The model does not currently represent these anisotropic effects as they are difficult to discern from ground-based radar, but the results of Hinkelman (2003) suggest that manipulation of E_3 could enable them to be simulated in an analogous way to the anisotropic mixing method discussed in section 3(b).

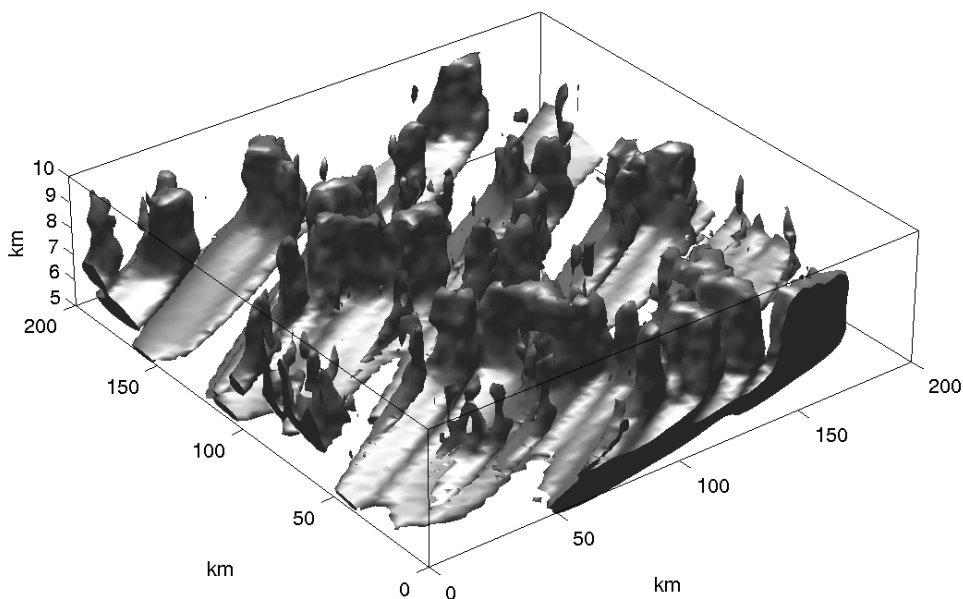


Figure 9. 3-D visualization of the 0.2 g m^{-3} ice-water content isosurface, for a simulation of the 27 December 1999 case.

5. RADIATIVE PROPERTIES OF INHOMOGENEOUS CIRRUS CLOUDS

(a) Overview of radiation calculations performed

In this section the Edwards and Slingo (1996) radiation code is used to explore the radiative properties of the three cirrus cases introduced in the previous section. While three cases is clearly not sufficient to encompass the behaviour of all cirrus globally, the properties highlighted will be common to many other cirrus clouds.

The independent column approximation (ICA) is assumed, i.e. the model is run separately for each profile of the simulated cloud with no horizontal transport of photons. DiGiuseppe and Tompkins (2003) found that for boundary-layer clouds ICA performed well compared to full 3-D radiation calculations in terms of calculating domain-averaged fluxes, except for broken clouds with a dominant scale of less than 10 km. As cirrus clouds have a dominant scale of around 50 km, ICA is likely to be adequate, although the longer mean free photon path length in cirrus means that this assertion will need to be tested in a future study.

For all the runs we use a solar zenith angle of 60° (leading to a top-of-atmosphere downwelling solar irradiance of 685 W m^{-2}), a surface albedo of 0.2 and no low cloud present. The long-wave calculations employed 9 spectral bands and used the Slingo and Schrecker (1982) parametrization for the ice-particle properties (with inclusion of long-wave scattering), while the short-wave used 24 bands together with the Kristjánsson *et al.* (2000) scheme. To increase the speed of the radiation computations, the cirrus clouds were generated on a smaller grid than before of $64 \times 64 \times 64$ pixels, measuring 100 km in each horizontal direction and extending vertically just over the height range containing cloud. This yields a horizontal resolution of 1.56 km and between 45 and 110 m in the vertical (depending on the case), encompassing the important range of horizontal scales from the 2–5 km width of the smallest fallstreak to the 50 km outer scale.

TABLE 2. MEAN TOP-OF-ATMOSPHERE REFLECTED SHORT-WAVE RADIATION MINUS CLEAR-SKY VALUE (Δ RSR) AND MEAN OUTGOING LONG-WAVE RADIATION MINUS CLEAR-SKY VALUE (Δ OLR) IN UNITS OF W m^{-2} FOR THE THREE CIRRUS CASES CONSIDERED IN THE TEXT. THE CLEAR-SKY VALUES ARE $\text{RSR}_{\text{cs}} = 135.6 \text{ W m}^{-2}$ AND $\text{OLR}_{\text{cs}} = 274.1 \text{ W m}^{-2}$. THE RESULTS ARE SHOWN FOR SEVERAL SEPARATE CALCULATIONS, ONE USING THE 2-D IWC FIELD OBSERVED BY THE RADAR, FOUR USING SIMULATED 3-D CLOUD FIELDS, AND TWO USING EQUIVALENT PLANE-PARALLEL CLOUDS WITH DIFFERENT OVERLAP ASSUMPTIONS.

Case	24 June 1999		27 Aug 1999		27 Dec 1999	
	Δ RSR	Δ OLR	Δ RSR	Δ OLR	Δ RSR	Δ OLR
Observed 2-D cloud field, independent column approximation	+43.6	-24.3	+181.7	-84.2	+292.8	-104.0
Simulated 3-D cloud fields, independent column approximation						
Control simulation: observed shear	+39.0	-20.9	+177.6	-78.9	+291.5	-103.4
Observed shear, no mixing	+26.4	-14.3	+165.5	-74.1	+288.7	-102.6
No shear	+31.8	-17.1	+157.6	-71.8	+271.0	-102.3
No shear, no mixing	+20.1	-11.0	+133.3	-61.7	+258.4	-99.9
GCM-type plane-parallel radiation schemes						
Maximum-random overlap	+46.5	-30.0	+232.9	-98.3	+303.8	-112.7
Exact overlap	+89.2	-51.5	+235.8	-98.7	+305.3	-113.4

See text for further explanation.

The cloud profiles were embedded in the McClatchey *et al.* (1972) standard US atmosphere. The pseudo-random number generator used by the model was seeded with the same value for each run in order that the same initial 3-D fractal field was used to obtain the realistic cloud as described in section 3(a). This ensured that the experiments were sensitive to the subtle effects of wind shear and mixing without being overwhelmed by statistical noise.

We assume a constant effective radius r_e of $50 \mu\text{m}$ throughout the cloud, which corresponds to a mean maximum dimension (the size parameter used by the Kristjánsson *et al.* (2000) scheme) of $225 \mu\text{m}$. Although the stochastic model does have the capability to simulate varying effective radius with a prescribed PDF and correlation with IWC (following the method of Evans and Wiscombe 2004), the purpose of this study is to examine the effect of cloud macrophysical rather than microphysical properties. The resulting domain-mean visible optical depths are given in Table 1. In all the calculations that follow the total ice content of the domain, and hence the mean optical depth, are held fixed for each case. In this way we may test the effect on mean fluxes and heating rates of the *distribution* of ice rather than the total amount.

We first compare ICA calculations performed directly on the retrieved 2-D IWC fields with those from the corresponding 3-D model simulations. In each case the mean top-of-atmosphere (TOA) reflected short-wave radiation (RSR) and mean TOA outgoing long-wave radiation (OLR) are computed. The clear-sky values are then subtracted to yield the cloud ‘effect’ or ‘forcing’ in the short-wave and long-wave, which we denote Δ RSR and Δ OLR. The first two lines of Table 2 show that the simulations agree with the observations to around 5 W m^{-2} , which is of the same order as the difference between two simulations using the same set of input statistics but a different set of random numbers for the phases of the Fourier amplitudes.

(b) *The effect of wind shear on mean fluxes via fallstreak orientation*

We next investigate the effect of wind shear on mean TOA fluxes, via its effect on fallstreak orientation. Table 1 shows the wind shear calculated over the height range corresponding to the 25th and 75th percentiles of horizontal-mean IWC, which may be

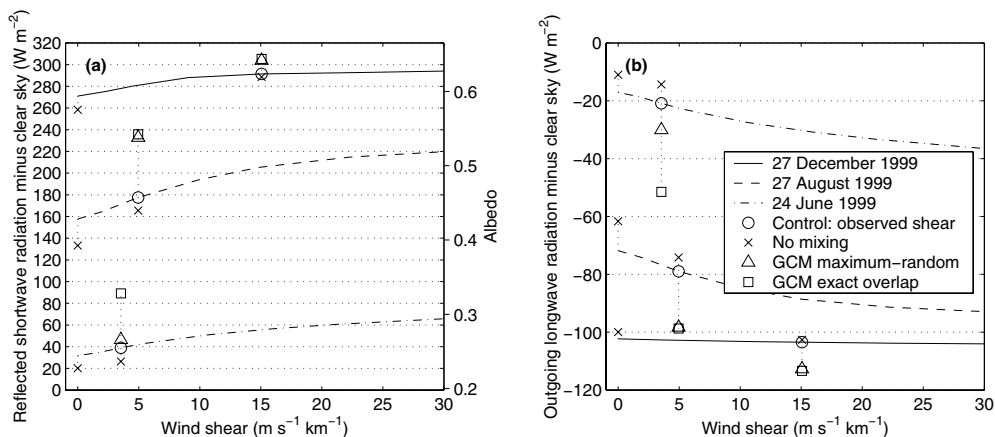


Figure 10. (a) Mean top-of-atmosphere reflected short-wave radiation and (b) outgoing long-wave radiation, minus the clear-sky values, as functions of wind shear between the 25th and 75th percentiles of horizontal-mean ice-water content for the three simulated cases (solid, dashed and dot-dashed lines). The circles indicate the actual wind shear for each case. Also shown are the results when the mixing effect of cirrus is removed (crosses) and for the equivalent plane-parallel clouds (triangles and squares), with the vertical dotted lines indicating which of the three cases they refer to. The numerical values are given in Table 2.

regarded as the region where the orientation of the fallstreaks will have the most effect on radiative transfer. For each case a sequence of runs of the model was performed in which the wind profile was scaled such that the wind shear over this height range varied between 0 and $30 \text{ m s}^{-1} \text{ km}^{-1}$.

The results are plotted versus wind shear in Fig. 10, with the circles indicating the results for the control experiment with an unmodified wind profile. It can be seen that the greatest effect in both the short-wave and long-wave is for the 27 August 1999 case, in which increasing the shear from 0 to $15 \text{ m s}^{-1} \text{ km}^{-1}$ results in a decrease in ΔOLR of 17 W m^{-2} and an increase in ΔRSR of 48 W m^{-2} (or equivalently an increase of mean short-wave albedo from 0.43 to 0.50). These may be expressed as an increase in the cloud radiative effect by 30% in the short-wave and 24% in the long-wave.

Figures 11(a) and (b) show the TOA albedo for these two values of wind shear, and can be considered to be similar to what would be observed by a high-resolution satellite-borne broadband imager. Figures 11(c) and (d) show slices through the domain parallel to the generating-layer wind vector, simulating what would be seen from a ground-based radar. It can be seen that the effect of wind shear and the associated extended fallstreaks is essentially to fill in the gaps where the local optical depth was very low, such that average albedo is increased despite the domain-mean optical depth remaining constant. This may equivalently be explained by the fact that wind shear tends to narrow the PDF of optical depth, coupled to the curvature in the optical depth to albedo relationship (Harshvardhan and Randall 1985; Carlin *et al.* 2002). The dependence of the long-wave fluxes on wind shear is for essentially the same reason, but the curvature is between optical depth and emissivity (Pomroy and Illingworth 2000). It should be noted that, in contrast to cirrus, the effect of stratocumulus inhomogeneity on long-wave fluxes is insignificant as the higher optical depth leads to the clouds behaving as black bodies, and the emission temperature is much more similar to that of the surface beneath.

The 24 June 1999 case showed a lower absolute effect of wind shear, although the *relative* effect was greater in both the short-wave and long-wave, increasing by around 75% in response to an increase in shear from 0 to $15 \text{ m s}^{-1} \text{ km}^{-1}$ due to the associated

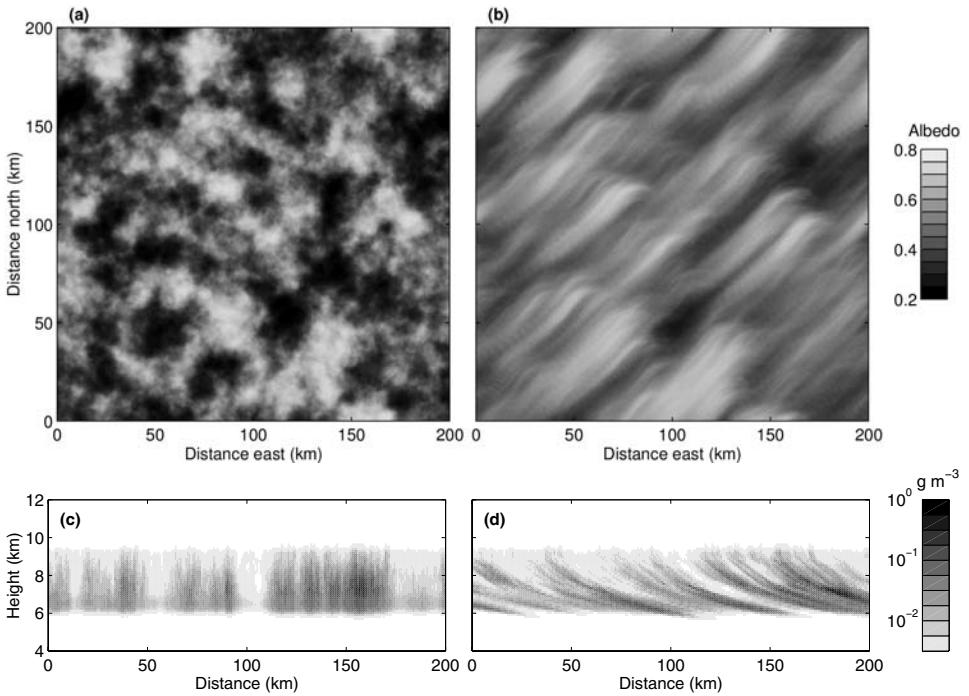


Figure 11. (a) Top-of-atmosphere short-wave albedo for a simulation of the 27 August 1999 case but with no wind shear, (b) albedo for the same case but with a wind shear of $15 \text{ m s}^{-1} \text{ km}^{-1}$, (c) time–height slice of ice-water content (IWC) taken diagonally through the domain for the no-shear simulation, and (d) the IWC slice for the sheared simulation. This figure has been produced using a higher resolution (256×256 pixels in the horizontal) and a larger domain than in the ICA calculations (see text), and albedo α has been calculated from visible optical depth δ , using $\alpha = 0.2 + 0.525\delta/(\delta + 3.5)$, which reproduces the albedo predicted by the Edwards and Slingo (1996) code in this configuration to within 0.02.

increase in cloud cover. In the case of 27 December 1999, the mean optical depth was much higher and in the long-wave was behaving very much as a black body, with only a 1 W m^{-2} difference between shears of 0 and $15 \text{ m s}^{-1} \text{ km}^{-1}$. The corresponding change in the short-wave was 21 W m^{-2} , less than the effect on 27 August 1999 because the albedo response to increasing optical depth was beginning to saturate.

In summary, wind shear can have a very substantial effect on the effect of a cirrus cloud on mean fluxes in both the long-wave and the short-wave. In this experiment we have kept the properties at each layer constant and simply moved layers horizontally with respect to one another, but it should be noted that in reality wind shear will be likely to affect the properties of the cloud at each layer via shear-induced instability, and the change in the radiation itself will feed back on the cloud properties (Dobbie and Jonas 2001).

(c) *The effect of horizontal mixing on mean fluxes*

One of the effects of wind shear not investigated in the previous section was its promotion of horizontal mixing. Mixing exhibits itself in two ways, a steepening of the slope of the power spectrum (see Figs. 2(b) and 3) and a corresponding reduction in fractional standard deviation (Fig. 2(d); Hogan and Illingworth 2003). Here we investigate the role of mixing by attempting to remove its effects from the cirrus simulations. This is done by forcing the slope of the power spectra to be $-5/3$ at all

heights, but keeping E_1 the same for $k < k_{\text{outer}}$; essentially the spectra are pivoted from the point where they intercept the scale break marked in Figs. 3 and 4(c). Associated with this is an increase in $\sigma_{\ln \text{IWC}}$ which may be calculated directly from the new spectra. The value of $\overline{\ln \text{IWC}}$ is adjusted to ensure that the mean IWC at each level remains constant, using the property of log-normal distributions that

$$\overline{\text{IWC}} = \exp(\overline{\ln \text{IWC}} + \sigma_{\ln \text{IWC}}^2/2). \quad (14)$$

Two experiments were performed for each case, one in which mixing was removed from a simulation in which the observed wind shear was still used to orient the fallstreaks, and the other with mixing removed from a simulation with no shear and hence vertically oriented fallstreaks. The effects on ΔRSR and ΔOLR are shown by the crosses in Fig. 10 (which are joined by vertical dotted lines to the corresponding simulations with mixing). It can be seen that removing the effects of mixing causes a decrease in the radiative effect of a cloud, due to the associated increase in variance of optical depth across the domain. The effect was strongest for the 27 August 1999 case with no wind shear, in which the short-wave effect was reduced by 24 W m^{-2} and the long-wave effect by 10 W m^{-2} , i.e. around half as large as the effect of changing fallstreak orientation found in the previous section.

(d) *Comparison with the representation of clouds in general-circulation models*

Next we investigate the fluxes that would be diagnosed by a general-circulation model (GCM), assuming it to correctly predict grid-box-mean IWC, cloud fraction (i.e. the fraction of pixels at each level with $\text{IWC} > 0.001 \text{ g m}^{-3}$) and effective radius, but to represent IWC as horizontally homogeneous within the cloudy fraction of the box. In the first experiment we follow the radiation schemes in most current GCMs and apply the ‘maximum-random’ overlap assumption (Geleyn and Hollingsworth 1979) whereby the clouds in adjacent layers are maximally overlapped, but if a layer of clear sky separates two layers of cloud then these layers are randomly overlapped. In the second experiment the IWC within cloud is still horizontally homogeneous, but the exact overlap configuration in the control simulation of the stochastic model is used, representing a GCM with an accurate cloud overlap scheme. The experiments are performed at the same vertical resolution as before; this is much better than the resolution of current GCMs, but when it is degraded by a factor of four the fluxes are the same to within 0.5 W m^{-2} in the short-wave and 0.2 W m^{-2} in the long-wave.

The results for maximum-random overlap and ‘exact overlap’ are given in Table 2 and shown in Fig. 10 by the triangles and squares, respectively. For clarity they are shown as points immediately above or below the circle indicating the control experiment, but note that the ‘maximum-random’ simulation is actually independent of wind shear. In all three cases the GCM schemes tend to overestimate the radiative effect of the cloud, but to varying degrees. In the 27 August and 27 December 1999 cases the two GCM schemes perform equally poorly. This is because, as can be seen in Fig. 7(b), cloud fraction is very close to unity at all heights so the overlap configuration is virtually irrelevant and both schemes have the same errors stemming from the failure to represent horizontal inhomogeneity.

In the 24 June 1999 case, the maximum-random overlap assumption performs reasonably well with errors of less than 10 W m^{-2} in both the long-wave and the short-wave. By contrast, the more realistic ‘exact overlap’ calculation results in a worse performance, with the short-wave and long-wave effects of the cloud being more than a factor of two too large. The reason is that the maximum-random overlap assumption

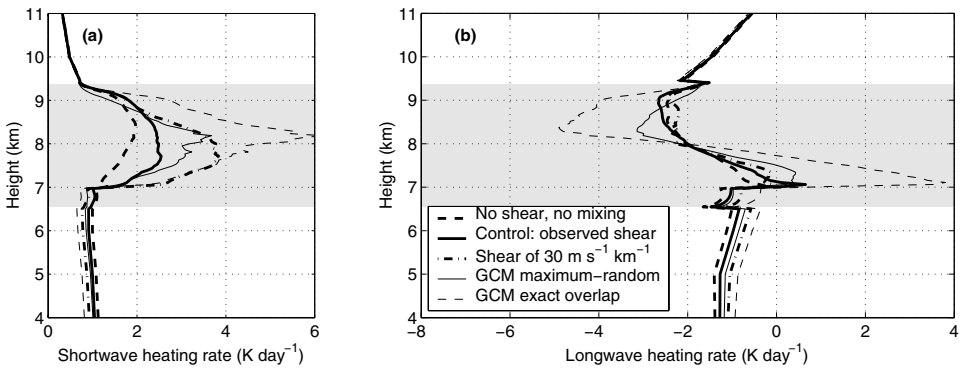


Figure 12. Domain-averaged (a) short-wave and (b) long-wave heating rates for the 24 June 1999 case. The grey-shaded area indicates the height range in which some cloud is present. The thick lines correspond to the full radiation calculations on simulations with three different values of shear, while the thin lines correspond to GCM-type calculations with two different assumptions regarding the subgrid distribution. Note that the clear-sky ‘notches’ of around 1 K day^{-1} in the long-wave heating rate at 6.5 and 9.5 km are artifacts of the change to a much higher vertical resolution in the radiation calculation over this height range.

has two partially compensating errors: an overestimation of the radiative effect due to its inability to represent horizontal cloud inhomogeneity, and an underestimation due to the clouds being too vertically aligned (i.e. the overlap should be more random; see Hogan and Illingworth 2000). In the cases shown the former effect is dominant. This leads to the conclusion that implementation of an improved overlap scheme along the lines of Hogan and Illingworth (2000) might actually result in the radiative biases being worsened, as it would correct one of the errors but not the other. Hence, only with the representation of both subgrid-scale fluctuations in water content and their overlap (e.g. Hogan and Illingworth 2003; Pincus *et al.* 2003; Räisänen *et al.* 2004) are accurate fluxes likely to be predicted by GCMs when inhomogeneous cirrus is present.

(e) Heating rates

Figures 12–14 show the mean short-wave and long-wave heating-rate profiles calculated from the full 3-D cloud fields and the two GCM representations. In the first two cases the distribution of ice within the domain has a substantial effect; the absence of shear and the associated absence of mixing results in a notable reduction in the magnitude of the heating or cooling rate compared to the control simulation. On the other hand, the elongation of fallstreaks associated with increased shear generally results in an increase in the heating or cooling rate at any given height. In the third case (Fig. 14), wind shear has a much more modest effect, as at the altitude of the fallstreaks, the radiative dependence on the cloud distribution has almost saturated.

Figure 12 indicates that the short-wave heating rate for the maximum-random assumption on 24 June 1999 is not dissimilar to the corresponding profile for a shear of $30 \text{ m s}^{-1} \text{ km}^{-1}$, due to the compensating errors discussed in section 5(d). The exact overlap simulation, however, results in a gross overestimate, as only one of the two compensating errors has been corrected.

In Figs. 13 and 14 the two GCM representations perform very similarly, with both overestimating the magnitude of the heating or cooling by up to a factor of two. This is despite the fact that, in the 27 December 1999 case, the effect of the cloud on mean TOA fluxes was overestimated by less than 10% (see Fig. 10). The reason is that in this case neither of the GCM schemes have come close to representing the strong

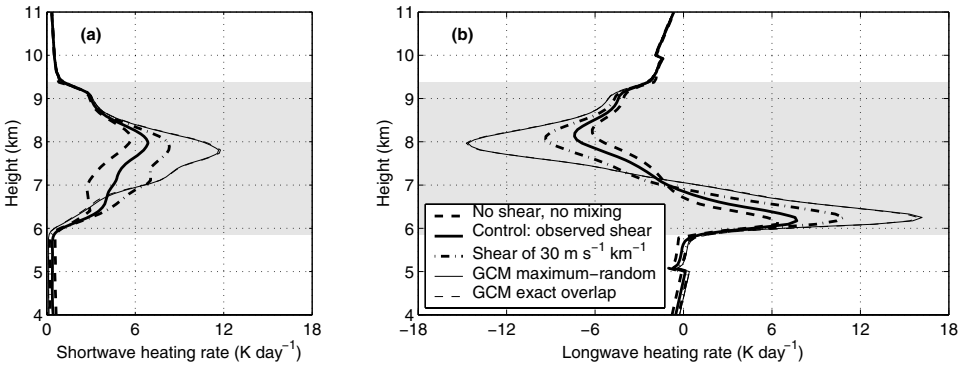


Figure 13. As Fig. 12 but for the 27 August 1999 case. Note that the maximum-random and exact overlap curves are almost coincident. The notches in the long-wave profile at 5 and 10 km are again due to resolution changes.

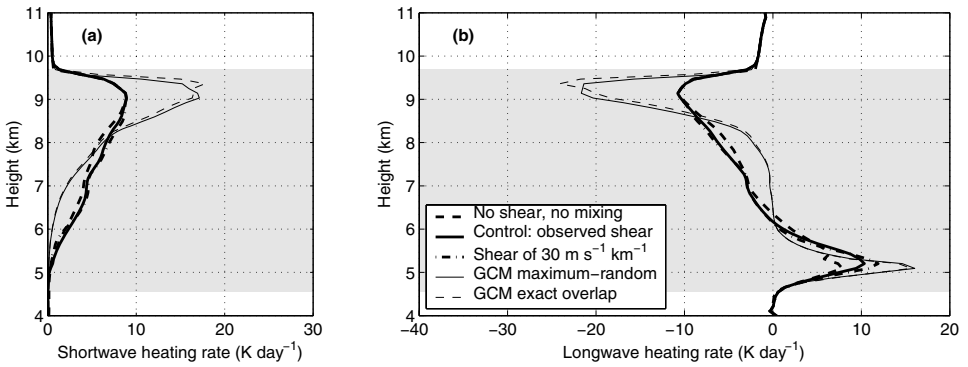


Figure 14. As Fig. 12 but for the 27 December 1999 case.

cloud-top inhomogeneities evident in Figs. 1, 2(d) and 8, but rather have smoothed out IWC uniformly across the domain. This has prevented incoming solar radiation from penetrating as far into the cloud from above, and similarly has reabsorbed long-wave radiation emitted lower in the domain. When the net (i.e. short-wave plus long-wave) heating rates are considered, the control simulation results in the mean short-wave and long-wave heating rates cancelling out to within 2.5 K d^{-1} at all heights above 7 km. By contrast, the maximum-random overlap assumption predicts a net cooling of 6 K d^{-1} at 9.5 km but a warming of 4 K d^{-1} one kilometre lower in the profile. This would be likely to lead to erroneous generation of instability near cloud top. Of course, the exact values stated here are a function of the solar zenith angle assumed, but for all solar zenith angles the net heating rate predicted by a GCM would be very different from a simulation with the inhomogeneities represented.

6. CONCLUSIONS

In this paper a stochastic model has been described for generating realistic 3-D cirrus cloud fields from radar time–height cross-sections using efficient Fourier transform techniques. Unique to the model is its ability to represent 3-D fallstreak structure, variable grid resolution in the horizontal and vertical direction via manipulation of the spectral energy matrix, and its reproduction of the characteristic features of observed

power spectra in cirrus. Horizontal power spectra from three radar events revealed some intriguing characteristics. A steepening of the slope of the power spectrum from close to $-5/3$ at cloud top (indicative of turbulence) to values as low as -3.5 near cloud base was attributed to variable particle fall speeds in the presence of wind shear leading to horizontal mixing preferentially at smaller scales. A scale break was observed at around 50 km, with the spectra becoming flat at larger scales.

Radiative-transfer calculations on simulated clouds based on real events have demonstrated the strong effect of wind shear on both short-wave and long-wave fluxes, via its effect on fallstreak orientation and horizontal mixing. This highlights the importance of cirrus inhomogeneity for climate and the need to represent it adequately in large-scale models. Even for optically thick clouds for which top-of-atmosphere fluxes might be predicted relatively well by GCM radiation schemes, the failure to represent the strong inhomogeneities at cloud top could lead to the heating-rate profile being very poorly predicted. We find that using accurate cloud overlap information but retaining the plane-parallel assumption could result in a worse representation of the radiative effects of cirrus in GCMs, highlighting the need to represent cloud inhomogeneity as well as overlap. In contrast to cirrus, the effect of stratocumulus inhomogeneity on long-wave fluxes is virtually insignificant as the emission temperature is much more similar to that of the surface beneath, and the higher optical depth leads to the clouds behaving as black bodies.

Some of the simplifications made in this study could easily be relaxed. Variable effective radius is possible by applying a method similar to Evans and Wiscombe (2004) and generating two isotropic 3-D fractals with a specified correlation between them, then manipulating one to yield IWC and the other to yield effective radius. Similarly it is possible to generate distributions other than log-normal by interpreting the final Gaussian field as the index to a look-up table. Three-dimensional radiative-transfer calculations are planned to investigate the role of horizontal photon transport in cirrus. There is also a need to extend this study from midlatitude cirrus to tropical anvils, for which Buschmann *et al.* (2002) reported considerably more horizontal inhomogeneity.

ACKNOWLEDGEMENTS

We thank Malcolm Brooks for assistance in running the radiation code and Keith Shine, John Thurnburn and one of the anonymous reviewers for providing valuable comments on the original manuscript. The Rutherford Appleton Laboratory is thanked for the use of the Galileo radar, which was developed for the European Space Agency by Officine Galileo, the Rutherford Appleton Laboratory and the University of Reading under ESTEC Contract 10568/NL/NB. The Met Office provided the radiosonde data. SFK was supported by a Natural Environment Research Council studentship, award number NER/S/M/2002/10650.

APPENDIX A

Treatment of incomplete datasets

The stochastic model produces log-normal distributions of ice-water content and represents broken clouds by simply setting values lower than a certain threshold to zero. It requires as input the mean and standard deviation of this hypothetical underlying (and unbroken) distribution of \ln IWC. In this appendix we show how these parameters may be estimated from a dataset in broken cloud.

The problem is considered in general terms: we have a series of measurements x (which could represent \ln IWC or radar reflectivity in dBZ), for which we would like to estimate the mean and standard deviation of the underlying distribution, \bar{x} and σ_x . In a broken cloud field (or due to the sensitivity of the instrument), only a fraction f of the data series contains valid values; for x less than the minimum detectable or ‘threshold’ value, x_c , no value is recorded. If we suppose that the underlying probability density function $P(x)$ is a normal:

$$P(x) = \frac{1}{\sigma_x \sqrt{2\pi}} \exp\left\{-\frac{1}{2}\left(\frac{x - \bar{x}}{\sigma_x}\right)^2\right\}, \tag{A.1}$$

then from f , x_c and the mean of the detected values \bar{x}' , we can estimate \bar{x} and σ_x . The detected fraction f is given by

$$f = \int_{x_c}^{\infty} P(x) dx = \Phi\left(\frac{\bar{x} - x_c}{\sigma_x}\right), \tag{A.2}$$

where $\Phi(x)$ is the standard integral of a normal distribution, defined as

$$\Phi(x) = \frac{1}{\sqrt{2\pi}} \int_{-\infty}^x \exp\left(-\frac{t^2}{2}\right) dt. \tag{A.3}$$

The mean of the detected values of x is

$$\bar{x}' = \frac{\int_{x_c}^{\infty} x P(x) dx}{\int_{x_c}^{\infty} P(x) dx} = \frac{1}{f \sigma_x \sqrt{2\pi}} \int_{x_c}^{\infty} x \exp\left\{-\frac{1}{2}\left(\frac{x - \bar{x}}{\sigma_x}\right)^2\right\} dx. \tag{A.4}$$

With a change of variables we obtain

$$\bar{x}' = \bar{x} + \frac{\sigma_x}{f \sqrt{2\pi}} \exp\left\{-\frac{1}{2}\left(\frac{x_c - \bar{x}}{\sigma_x}\right)^2\right\}. \tag{A.5}$$

Thus we have two equations (A.2) and (A.5) and two unknowns. We use the inverse function of (A.3), Φ^{-1} , to transform (A.2), and denote the result A :

$$A = \frac{\bar{x} - x_c}{\sigma_x} = \Phi^{-1}(f) = \sqrt{2} \operatorname{erf}^{-1}(2f - 1). \tag{A.6}$$

Note that we have also expressed the result in terms of the inverse error function, erf^{-1} , as routines for computing it tend to be more widely available than for Φ^{-1} . Substituting (A.5) we obtain

$$B = \frac{\bar{x}' - \bar{x}}{\sigma_x} = \frac{1}{f \sqrt{2\pi}} \exp\left(-\frac{A^2}{2}\right). \tag{A.7}$$

Rearranging (A.6) and (A.7) yields the solution for \bar{x} and σ_x :

$$\bar{x} = x_c + \frac{\bar{x}' - x_c}{1 + B/A}, \quad \sigma_x = \frac{\bar{x}' - x_c}{A + B}. \tag{A.8}$$

As f approaches unity this method is not the best way of estimating \bar{x} and σ_x because f becomes more an indicator of the lower tail of the distribution, rather than a good indicator of the width of the distribution σ_x , which is what is required.

An alternative approach that we implement when $f > 0.8$ is to assume that the median of the underlying distribution is equal to the mean \bar{x} . Since we have more than half the values, the median is easy to determine. The width of the underlying distribution σ_x may be estimated by first calculating the mean of the data greater than \bar{x} , which we denote $\bar{x}'_{1/2}$:

$$\bar{x}'_{1/2} = \frac{\int_{\bar{x}}^{\infty} x P(x) dx}{\int_{\bar{x}}^{\infty} P(x) dx}. \quad (\text{A.9})$$

From (A.5) it is easy to show that $\bar{x}'_{1/2} = \bar{x} + \sigma_x \sqrt{2/\pi}$. Hence σ_x may be estimated from \bar{x} and $\bar{x}'_{1/2}$.

APPENDIX B

Formulation of the 3-D power spectrum

Here we derive the expressions for E_3 given in (7)–(13), by considering how (5) changes when it is converted to discrete form in different ranges of k . Each region of wave-number space depicted in Fig. 4(b) is considered in turn.

(i) *Region III: 3-D behaviour.* We first consider Region III, corresponding approximately to scales between $2\Delta x$ and the vertical domain size L_z . In this region the behaviour is fully three-dimensional, so we may use (6). This equation is therefore repeated in (9).

(ii) *Region IV: Quasi-1-D behaviour (z direction).* This region consists of scales smaller than twice the horizontal grid size, $2\Delta x$, so here the only variations are in the z direction where the resolution is higher, and the behaviour may be regarded as quasi-one-dimensional. This can be seen in Fig. 4(a), by the edge of the wave-number domain at $\pm K_x$, indicating that no fluctuations with absolute wave number in the x direction larger than K_x are possible, and similarly in the y direction.

We consider the limit $k \gg K_x$ (i.e. towards the top and bottom of the wave-number domain in Fig. 4(a)) and seek a solution of the form $E_3 = \widehat{E}_3 k^{-\nu}$. The k_z form of (5) is taken, replacing the infinite limits appropriately as follows:

$$E_1(k_z) = \int_{-K_x}^{K_x} \int_{-K_y}^{K_y} \widehat{E}_3 k^{-\nu} dk_y dk_x. \quad (\text{B.1})$$

Since $k \simeq k_z$ in this region and k is almost independent of the much smaller k_x and k_y , (B.1) becomes

$$E_1(k) = 4K_x K_y \widehat{E}_3 k^{-\nu}. \quad (\text{B.2})$$

Thus from (4) we have $\nu = \mu$ and $\widehat{E}_3 = \widehat{E}_1 (4K_x K_y)^{-1}$, and hence E_3 has the form given by (10). In reality E_3 should vary smoothly between the limits of full 3-D behaviour given by (9) and the quasi-1-D behaviour of (10). However, for simplicity we assume that there is a sharp transition from one regime to the other at wave number k_{III} . Equating the two expressions for E_3 at this wave number:

$$\frac{\widehat{E}_1 \mu}{2\pi} k_{\text{III}}^{-\mu-2} = \frac{\widehat{E}_1}{4K_x K_y} k_{\text{III}}^{-\mu}, \quad (\text{B.3})$$

leads to $k_{\text{III}} = \sqrt{2\mu/\pi} K_x$, as given by (13). Typically in cirrus μ is close to 2, for which $k_{\text{III}} = 1.13K_x$. The sharp transition of two powers of k between Regions III and IV is apparent in Fig. 4(b) and has the result that the 1-D power spectrum in the z direction

(indicated in Fig. 4(c)) is somewhat underestimated in the vicinity of k_{III} . However, this is not of great concern as the vertical power spectrum in the frame of reference of a fallstreak has never been measured in cirrus clouds.

(iii) *Region II: Quasi-2-D behaviour (x - y plane).* At scales larger than L_z , fluctuations are only possible in the x and y directions, so the behaviour becomes quasi-two-dimensional. As illustrated in Fig. 4(a), in wave-number space this is manifested as spheres of radius $k < \Delta k_z$ only encompassing a single plane of discrete points (lying on the $k_z = 0$ surface). We again seek a solution of the form $E_3 = \widehat{E}_3 k^{-\nu}$, and in the limit of $k \ll \Delta k_z$, (5) reduces to

$$E_1(k_x) = \Delta k_z \int_{-\infty}^{\infty} \widehat{E}_3 k^{-\nu} dk_y, \quad (\text{B.4})$$

and similarly for $E_1(k_y)$. Note that, because the energy E_3 is so much less for points in the adjacent planes $k_z = \pm \Delta k_z$ than in the $k_z = 0$ plane, we have been able to replace the integral in the k_z direction with the effective width of this plane in discrete wave-number space, Δk_z . Because $k_z = 0$ we have $k = (k_x^2 + k_y^2)^{1/2}$, which when substituted into (B.4) yields the solution given by (8). As above, a sharp transition is assumed between the quasi-2-D behaviour described by (8) and the full 3-D behaviour of (9). Equating E_3 at wave number k_{II} :

$$\frac{\widehat{E}_1 \mu}{2\pi} k_{\text{II}}^{-\mu-2} = \frac{\widehat{E}_1}{\Delta k_z \sqrt{\pi}} \frac{\Gamma\{(\mu+1)/2\}}{\Gamma(\mu/2)} k_{\text{II}}^{-\mu-1}, \quad (\text{B.5})$$

yields the expression for k_{II} given by (12). For the case of $\mu = 2$, this reduces to $k_{\text{II}} = 2\Delta k_z/\pi = 0.64\Delta k_z$. As is apparent in Figs. 4(b) and (c), the fact that the change in slope between the two regions is only one power of k has led to the resulting 1-D power spectrum in the x (or y) direction more closely approximating the ‘requested’ spectrum in the vicinity of k_{II} than was the case of the z spectrum in the vicinity of k_{III} .

(iv) *Region I: Outer scale.* In the observed cirrus power spectra presented in section 2(c), the outer scale was present as smooth transition from a slope of $-\mu$ to E_1 being independent of k , over less than a decade of k . Rather than attempting to characterize the shape of this transition exactly, we note that simply setting E_3 to a constant for $k < k_{\text{outer}}$ results in the simulated 1-D spectrum having a form very close to that observed, as shown in Fig. 4(c). For Region I we therefore set the transition wave number to $k_{\text{I}} = k_{\text{outer}}$ and for wave numbers less than this adopt a constant value of E_3 that matches the Region II value at k_{outer} , as given by (7).

REFERENCES

- Buschmann, N., McFarquhar, G. M. and Heymsfield, A. J. 2002 Effects of observed horizontal inhomogeneities within cirrus clouds on solar radiative transfer. *J. Geophys. Res.*, **107**, doi: 10.109/2001JD001273
- Cahalan, R. F., Ridgeway, W., Wiscombe, W. J., Bell, T. L. and Snider, J. B. 1994 The albedo of fractal stratocumulus clouds. *J. Atmos. Sci.*, **51**, 2434–2455
- Carlin, B., Fu, Q., Lohmann, U., Mace, G. G., Sassen, K. and Comstock, J. M. 2002 High-cloud horizontal inhomogeneity and solar albedo bias. *J. Climate*, **15**, 2321–2339
- Davis, A., Marshak, A., Wiscombe, W. and Cahalan, R. 1996 Scale invariance of liquid water distributions in marine stratocumulus—1. Spectral properties and stationarity issues. *J. Atmos. Sci.*, **53**, 1538–1558
- DiGiuseppe, F. and Tompkins, A. M. 2003 Effect of spatial organisation on solar radiative transfer in three dimensional idealized stratocumulus cloud fields. *J. Atmos. Sci.*, **60**, 1774–1794
- Dobbie, S. and Jonas, P. 2001 Radiative influences on the structure and lifetime of cirrus clouds. *Q. J. R. Meteorol. Soc.*, **127**, 2663–2682

- Edwards, J. M. and Slingo, A. 1996 Studies with a flexible new radiation code. 1: Choosing a configuration for a large-scale model. *Q. J. R. Meteorol. Soc.*, **122**, 689–719
- Evans, K. F. and Wiscombe, W. J. 2004 An algorithm for generating stochastic cloud fields from radar profile statistics. *Atmos. Res.*, **72**, 263–289
- Fu, Q., Carlin, B. and Mace, G. G. 2000 Cirrus horizontal inhomogeneity and OLR bias. *Geophys. Res. Lett.*, **27**, 3341–3344
- Geleyn, J. F. and Hollingsworth, A. 1979 An economical analytical method for the computation of the interaction between scattering and line absorption of radiation. *Contrib. Atmos. Phys.*, **52**, 1–16
- Harshvardhan and Randall, D. A. 1985 Comments on ‘The parameterization of radiation for numerical weather prediction and climate models’. *Mon. Weather Rev.*, **113**, 1832–1833
- Heymsfield, A. J. 1975 Cirrus uncinus generating cells and the evolution of cirriform clouds—2. The structure and circulations of the cirrus uncinus generating head. *J. Atmos. Sci.*, **32**, 809–819
- Hinkelman, L. M. 2003 ‘The effect of cumulus cloud field anisotropy on solar radiative fluxes and atmospheric heating rates’. PhD Thesis, The Pennsylvania State University
- Hogan, R. J. and Illingworth, A. J. 1999 The potential of spaceborne dual-wavelength radar to make global measurements of cirrus clouds. *J. Atmos. Oceanic Technol.*, **16**, 518–531
- 2000 Deriving cloud overlap statistics from radar. *Q. J. R. Meteorol. Soc.*, **126**, 2903–2909
- 2003 Parameterizing ice cloud inhomogeneity and the overlap of inhomogeneities using cloud radar data. *J. Atmos. Sci.*, **60**, 756–767
- Hogan, R. J., Bouniol, D., Ladd, D. N., O’Connor, E. J. and Illingworth, A. J. 2003 Absolute calibration of 94/95-GHz radars using rain. *J. Atmos. Oceanic Technol.*, **20**, 572–580
- Hogan, R. J., Mittermaier, M. P. and Illingworth, A. J. 2005 The retrieval of ice water content from radar reflectivity factor and temperature and its use in the evaluation of a mesoscale model. *J. Appl. Meteorol.* (in press)
- Kristjánsson, J. E., Edwards, J. M. and Mitchell, D. L. 2000 Impact of a new scheme for optical properties of ice crystals on climates of two GCMs. *J. Geophys. Res.*, **105**, 10063–10079
- Kuo, K. S., Welch, R. M. and Sengupta, S. K. 1988 Structural and textural characteristics of cirrus clouds observed using high spatial resolution LANDSAT imagery. *J. Appl. Meteorol.*, **27**, 1242–1260
- Lilly, D. K. 1983 Stratified turbulence and the mesoscale variability of the atmosphere. *J. Atmos. Sci.*, **40**, 749–761
- Liou, K.-N. 1986 Influence of cirrus clouds on weather and climate processes: A global perspective. *Mon. Weather Rev.*, **114**, 1167–1199
- McClatchey, R. A., Fenn, R. W., Selby, J. E. A., Volz, F. E. and Garing, J. S. 1972 ‘Optical properties of the atmosphere’. Report No. AFCRL72-0497, Air Force Cambridge Research Laboratories, Bedford, Mass, USA
- Marshak, A., Davis, A., Wiscombe, W. and Cahalan, R. 1997 Scale invariance of liquid water distributions in marine stratocumulus—2. Multifractal properties and intermittency issues. *J. Atmos. Sci.*, **54**, 1423–1444
- Marshall, J. S. 1953 Precipitation trajectories and patterns. *J. Meteorol.*, **10**, 25–30
- Mittermaier, M. P., Hogan, R. J. and Illingworth, A. J. 2004 Using mesoscale model winds for correcting wind-drift errors in radar estimates of surface rainfall. *Q. J. R. Meteorol. Soc.*, **30**, 2105–2123
- Pincus, R., Barker, H. W. and Morcrette, J.-J. 2003 A fast, flexible, approximate technique for computing radiative transfer in inhomogeneous cloud fields. *J. Geophys. Res.*, doi: 10.1209/2002JD003322
- Pomroy, H. R. and Illingworth, A. J. 2000 Ice cloud inhomogeneity: Quantifying bias in emissivity from radar observations. *Geophys. Res. Lett.*, **27**, 2101–2104
- Räisänen, P., Barker, H. W., Khairoutdinov, M. F., Li, J. N. and Randall, D. A. 2004 Stochastic generation of subgrid-scale cloudy columns for large-scale models. *Q. J. R. Meteorol. Soc.*, **130**, 2047–2068
- Slingo, A. and Schrecker, H. M. 1982 On the shortwave radiative properties of stratiform water clouds. *Q. J. R. Meteorol. Soc.*, **108**, 407–426
- Smith, S. A. and DelGenio, A. D. 2001 Analysis of aircraft, radiosonde, and radar observations in cirrus clouds observed during FIRE II: The interactions between environmental structure, turbulence, and cloud microphysical properties. *J. Atmos. Sci.*, **58**, 451–461